Journal of Environmental Chemical Engineering 3 (2015) 1847–1859

Contents lists available at ScienceDirect

Journal of Environmental Chemical Engineering

journal homepage: www.elsevier.com/locate/jece

Fabrication of Ag nanoparticles modified TiO_2–CNT heterostructures for enhanced visible light photocatalytic degradation of organic pollutants and bacteria

Mohamed Mokhtar Mohamed[a,*], G. Osman[b,c,d], K.S. Khairou[d]

[a] Chemistry Department, Faculty of Science, Benha University, Benha, Egypt
[b] Agricultural Genetic Engineering Research Institute (AGERI), Giza, Egypt
[c] Biology Department, Faculty of Applied Sciences, Umm Al Qura University, Makkah, Saudi Arabia
[d] Chemistry Department, Faculty of Applied Sciences, Umm Al Qura University, Makkah, Saudi Arabia

ARTICLE INFO

Keywords:
Silver nanoparticles
Ag_2O
TiO_2–CNTs composites
E. coli
Staphylococcus aureus
Growth suppression
DNA damage

ABSTRACT

TiO_2 synthesized using polymeric template consisting of polyethylene glycol and polyvinyl alcohol (Tev) and loaded with different wt% of Ag (2%, 6%) was exploited to create covalent bonds with carboxylate functionalized SWCNT/MWCNT moieties. The synthesized Ag free Tev–SWCNTs as well as Ag containing Tev–SWCNTs/MWCNTs have been characterized by UV–visible diffuse reflectance, powder XRD, HRTEM, and selected area electron diffraction (SAED), photoluminescence, Raman, FTIR and N_2 sorptiometry. The materials containing Ag displayed high photocatalytic activity towards degradation of rhodamine B dye under visible irradiation ($\lambda_{max} > 450$ nm). Specifically $TevAg_6$–SWCNT has shown the best performance (0.3 g/l catalyst, 20 ppm RhB conc. and 80 min reaction time) due to the synergistic effects derived from TiO_2/Ag°/SWCNT heteroarchitectures. The antibacterial activity of synthesized photocatalysts; under visible light irradiations, towards *Escherichia coli* and *Staphylococcus aureus* was tested by performing bacterial DNA and agar well diffusion method. The results revealed that $TevAg_6$–SWCNT was able to effectively kill both gram-positive and gram-negative bacteria. Although $TevAg_6$–SWCNT indicated higher E_g values (1.9 eV) than $TevAg_2$–MWCNT (1.75 cV) and they both exposed not only Ag° nanoparticles but also Ag_2O, the former sample confirmed more lethal action against bacterial growth as well as superior photodegradation activity. This was due to delaying the recombination of electrons and holes, increasing the S_{BET} value as well as decreasing the spherical nanoparticles of Ag° to 3 nm diameter. The mechanisms of the dye degradation and destruction of bacterial cell membranes indicate the efficacy of $^\bullet OH$ and $O_2^{\bullet -}$ as reactive radical intermediates in both processes.

Introduction

Carbon nanotubes (CNTs) have attracted considerable attention because of their excellent electrical, mechanical, magnetic properties, high surface areas and high chemical stability [1,2]. On the other hand, TiO_2 is used widely as a photocatalyst for solving environmental problems. In particular, it has been used to remove different chemical pollutants from water as well as from air [3–5]. However, the low photocatalytic efficiency has restricted the application of TiO_2, in practical water treatment [6–8], to be active only under ultraviolet irradiation. Composite materials containing CNTs and TiO_2 have attracted considerable attention owing to their unique properties. They are used widely in waste water treatment to remove a range of pollutants because of their large surface area, high adsorption capacity as well as shifting the photocatalytic reactions to take place under visible light irradiation [9,10]. Accordingly, when TiO_2 is coated on nanocarbon materials, the binding to pollutants will increase and the electron–hole recombination at the TiO_2–CNT interfaces is hindered by electron trapping and thus yields superior photocatalytic activities compared with individual analogue [11–13]. The morphology and structure of CNTs enable them to serve as specific templates for preparing metal nanoparticle–CNTs nanohybrids [14]. The combination of these two materials (i.e., CNTs and nanoparticle) is specifically useful when integrating the properties of the two components of the hybrid materials for use in catalysis, energy storage and nanotechnology [15]. Previous studies were carried out to find a low-cost, stable and effective nanocatalytic material as a substitute for noble metal catalysts. For instance Ag supported by

* Corresponding author.
E-mail address: mohmok2000@yahoo.com (M. Mokhtar Mohamed).

http://dx.doi.org/10.1016/j.jece.2015.06.018
2213-3437/

CNTs showed high electrocatalytic activity towards hydrazine oxidation [16]. As reported by Mohamed and Al-Sharif [17], the photocatalytic performance of Ag/TiO_2 for 4-nitrophenol reduction to 4-aminophenol, which was accomplished in less than 2 min reaction time, was also investigated and attributed to Ag°/Ag^{+} species formed at the interface of TiO_2. On the other hand, the higher activity of Ag°-modified mesoporous TiO_2 for herbicide degradation was predominant due to the presence of small Ag particles and to the interface formed between Ag and TiO_2 [18]. However, to date, little attention has been paid to the antibacterial properties of TiO_2–CNT composites.

In present days, resistance to commercially available antimicrobial agents by pathogenic microorganisms has been increasing at an alarming rate and has become a serious problem [19]. The inorganic agent silver has been employed as the most antimicrobial agent since ancient times to fight infection pathogens [20,21]. Accordingly, there are many in-vitro studies on antibacterial and antifungal properties of silver nanoparticles [22]. In daily life, human beings are often infected by microorganisms like bacteria, molds, viruses, etc. To impart sterility (e.g., hospital trays, contaminated water) and avoid infection (e.g., wound dressing), the use of antimicrobial agents is important. Research has been intensively carried out in antibacterial materials containing various natural and inorganic substrates [23–26] over the last few years. The mode of action of silver nanoparticles (Ag-NPs) on bacteria is probably the same as the silver ion that possesses higher toxicity comparatively [27]. It is believed that nanoscale Ag possesses superior reactivity than the bulk metallic counterpart because of high large surface area and varieties of engineered nanoscale Ag-modified nano-architectures [22–25]. In addition, Ag-NPs can bind to the DNA inside the bacterial cells, preventing its replication [28], or interact with the bacterial ribosome preventing translation [29], so Ag-NPs have attracted considerable attention as antimicrobial active materials [30]. Several techniques were used to manufacture Ag-NPs including chemical reduction of silver ions in aqueous solutions, with or without stabilizing agents, thermal decomposition in organic solvents and chemical and photo reduction in reverse micelles [31,32]. Most of these techniques are extremely expensive and capital intensive, they also involve the use of toxic, hazardous chemicals that may pose potential environmental and biological risks as well as is inefficient in materials and energy use [33]. In this study, the photocatalytic degradation of Ag/TiO_2–CNT towards rhodamine B (RhB) dye and the inactivation of bacteria; including *Escherchia coli* (*E. coli*) and *Staphylococcus aureas*, will be investigated together with the effect of nanoparticles on bacterial DNA. The effect of either Ag_2O and/or Ag° will be examined together with inspecting the reactive intermediates might be emitted while irradiating the photocatalysts and their lethal effects on the dye degradation and on the bacterial growth. Structural variations, optical and morphological properties were examined for the fabricated CNT/TiO_2 and Ag–CNT/TiO_2 composites. X-ray diffraction (XRD), transmission electron microscopy (SEM), energy dispersive X-ray (EDX), N_2 sorptiometry, FTIR, Raman, photoluminescence and UV–vis diffuse reflectance spectroscopy were used to characterize these synthesized photocatalysts.

Experimental

Catalysts preparation

Synthesis of mesoporous TiO_2–SWCNT and mesoporous TiO_2–MWCNT catalysts

TiO_2 nanoparticles were fabricated by self assembly method according to the following procedure. Briefly, polyethylene glycol ($HO(CH_2CH_2O)_nH$ – 0.01 M) and polyvinyl-alcohol ($CH_2—CH(OH)_n$ – 0.01 M) dissolved in a least amount of water (15 ml) in a weight ratio of 7:3 were mixed thoroughly. Titanium iso-propoxide ($Ti(OCH(CH_3)_2)_4$ – 29.3 ml) was added into the above mixture via a drop wise manner with vigorous stirring for half an hour at room temperature. The resulting reaction mixture was transferred into an autoclave lined with Teflon followed by hydrothermal treatment at 393 K for 48 h. After hydrothermal treatment, the product was recovered by centrifugation and then washed 3 times with deionized water. The solid was then dried overnight at 333 K and a portion of this sample was further calcined in air at 673 K for 6 h to remove the copolymer template. This sample was denoted as Tev, where the letter e expresses polyethylene glycol and v expresses polyvinyl-alcohol. Accordingly, the Tev (dried) catalyst was suspended individually in a mixture of ethanol–water and left under stirring for 2 h. This mixture was poured into single walled carbon nanotube SWCNT; purchased from Chengdu Organic Chemicals Co., Ltd., China (manufacture data: purity > 95; diameter < 8 nm; length 10–30 μm; $S_{BET} > 500\ m^2/g$) dissolved in ethanol to give ratios comprised of 20% SWCNT related to Tev, then sonicated at 313 K for 1.5 h. Then, it is left under stirring over night at room temperature and poured into a Teflon lined autoclave and heated under autogenous pressure at 433 K for 48 h. Finally, it is filtered, washed with absolute ethanol and distilled water, dried at 373 K overnight and then calcined at 673 K for 4 h. This sample was denoted as Tev–SWCNT.

Synthesis of mesoporous TiO_2–SWCNT and mesoporous TiO_2–MWCNT catalysts supported Ag nanoparticles

Different wt% of $AgNO_3$ at a ratio of either 2% or 6% took place before titanium iso-propoxide admission to prepare samples denoted as $TevAg_2$ and $TevAg_6$. Accordingly, $TevAg_2$ and $TevAg_6$ catalysts were suspended individually in a mixture of ethanol–water and left under stirring for 2 h. These mixtures were poured into the suspension of MWCNT (manufacture data: purity > 97; diameter < 12 nm; length 10–40 μm; $S_{BET} > 430\ m^2/g$) and SWCNT in ethanol to give ratios comprised of 20% MWCNT and SWCNT related to Tev then sonicated at 313 K for 1.5 h. Then, they were left under stirring over night at room temperature. The mixtures were afterwards poured into Teflon lined autoclaves and heated under autogenous pressure at 433 K for 48 h. Finally, they were filtered, washed with absolute ethanol and distilled water, dried at 373 K overnight and calcined at 673 K for 4 h. These samples are denoted as $TevAg_2$–SWCNT, $TevAg_2$–MWCNT and $TevAg_6$–SWCNT.

Catalyst characterization

X-ray diffraction analysis

X-ray diffraction analysis was performed on X-Ray diffraction (XRD) spectrometer Model XRD 8030 from Jeol Comp., Japan. Maximum power is 3 kW and the unit is equipped with rotating stage and thin layer accessories. The patterns were run with co-filtered CuKα radiation (λ = 1.79 Å) energized at 45 kV, and 10 mA. The samples were measured at room temperature in the range of $2\theta = 5–100^{\circ}$. The XRD phases present in the samples were identified with the help of ASTM Powder Data Files.

Transmission electron microscopy (TEM)

The nanostructured morphologies of the samples were examined using high resolution transmission electron microscopy (HRTEM) obtained by Tecnai G2 Supper Twin USA, with an accelerating voltage of 200 kV. The elemental composition of the composite material was investigated by energy-dispersive X-Ray attached to the TEM equipment. The average particle diameter (d) was calculated by the following formula: $d = \Sigma nidi/\Sigma ni$, where ni is the number of particle diameter di in a certain range, and Σni is more than 100 particles on TEM images of the sample. Computer-

assisted counting of nanoparticle images and automated image analysis based software package including KONTRON KS 400 (Zeiss-Kontron) was used.

Fourier transform infrared spectra (FT-IR)

The infrared spectra of the samples were recorded in the range of 400–1000 cm^{-1}. The method includes mixing few mg of a fine powder of the sample with KBr powder in agate mortar. The mixture was then pressed by means of hydraulic press. The transmission was automatically registered against wavenumber (cm^{-1}) using a PerkinElmer instrument (Spectrum GX), made in USA.

Nitrogen adsorption measurements

Nitrogen adsorption measurements were performed at liquid nitrogen temperature with a Micromeritics ASAP 2020 surface area and porosity analyzer. Prior to the measurements, the samples were degassed for half an hour at 363 K followed by 3 h at 473 K. Surface area was calculated using the BET (Brunauer–Emmett–Teller) interpretation of the nitrogen adsorption isotherm. The pore size distribution was determined from desorption branch of isotherm using BJH analysis. The pre-treatment conditions must remain sufficiently mild to avoid any modification of the textural characteristics of the sample but severe enough to obtain a good surface clean-up.

Ultraviolet–visible diffuse reflectance spectroscopy

Diffuse reflectance Ultraviolet–visible spectroscopy (UV–vis DRS) of powder samples was carried out at room temperature using a PerkinElmer Lambda-900 spectrophotometer in the range of 200–800 nm. The UV–vis spectra were processed with Microsoft Excel software, consisting of calculation of the Kubelka–Munk function, $F(R_\infty)$, which was extracted from the UV–vis DRS absorbance. The edge energy (E_g) for allowed transitions was determined by finding the intercept of the straight line in the low-energy rise of the plot of $[F(R_\infty)h\upsilon]^2$, for the direct allowed transition, vs. $h\upsilon$, where $h\upsilon$ is the incident photon energy.

Photoluminescence spectroscopy

The PL spectra were recorded by photoluminescence (PL) spectrometer (Spectro Fluorescence JASCO fp-6200) using 290 nm as excitation wavelength at room temperature via pulsed YAG:Nd laser excitation.

Photocatalytic degradation experiments

A high pressure Hg lamp of 125 W with a special UV cut off filter (λ = 450 nm) offering visible light source; with an average light intensity equal to 60 mW/cm^2, was placed at a specified position using a special rod in the reactor. A continuous cold water ($16 \pm 1\,^{\circ}C$) supply was maintained during the experiment to control the temperature of the reaction mixture. The photocatalyst (30 mg) was suspended in 100 ml aqueous solution of 20 mg/l rhodamine B (RhB). The solution was stirred in dark for 60 min to ensure the establishment of an adsorption–desorption equilibrium. Initial pH value of the liquid was 7.0 and was not adjusted subsequently. During the irradiation, 2 ml aliquots were removed at definite time intervals and analyzed with a Shimadzu UV-2350 spectrophotometer to measure RhB concentrations. In addition, TOC in the mixture was determined by using a high TOC II from Elementar Analysensysteme in order to investigate if the dye is photo-bleached or completely degraded. TOC analysis is attained via taking samples at the beginning, in the middle and at the end of the experiment.

For detecting the active species produced in the photocatalytic reaction, hydroxyl radicals ($^{\bullet}OH$), superoxide radical ($^{\bullet}O_2^-$) and holes (h^+) were explored by adding 1.0 mM isopropanol (IPA-aquencher of $^{\bullet}OH$), *p*-benzoquinone (BQ – a quencher of $^{\bullet}O_2^-$), and disodium (ethylenefinitrilo)tetraacetic acid (Na_2EDTA – a quencher of h^+), respectively.

Antibacterial test

Bacterial strains and growth conditions

Gram-negative bacteria *E. coli* and gram-positive bacteria *Streptomyces aureus* were grown and subcultured and maintained on nutrient agar and stored at 4 °C. For the experiment, a single colony of each organism was inoculated into 10 ml of LB broth and incubated overnight at 37 °C with shaking at 200 rpm. The optical density of the overnight culture was adjusted to that of a 0.5 spectrophotometer and diluted with LB broth to give a final working concentration of 1×10^6 CFU/ml.

Well diffusion method

Antibacterial activity of synthesized nanoparticles was tested against *Staphylococcus aureus* and *E. coli* by using well diffusion method. 100 and 50 μg/ml of the nanoparticles solutions were poured onto each of the wells at the core in all the plates. After incubation at 37 °C for 24 h, the different level of zone was measured. Negative control sterile liquid broth positive control as well as antibiotic disk test was tested in duplicate on each plate and each plate was analyzed in triplicate.

Antibiotic susceptibility testing

Antibiotic susceptibilities were tested by the disk diffusion method according to the guidelines of the British Society for Antimicrobial Chemotherapy (BASC, 2010) using nutrient agar (Oxoid). Six commercial antimicrobial disks (Mast Diagnostics, Bootle, UK) were used: erythromycin (60 μg/ml), rifampicin (15 μg/ml), penicillin G (2 IU), kanamycin (1000 g/ml), vancomycin (5 μg/ml) and oxacillin (μg/ml) (BioRad, Hercules, USA). *S. aureus* NCTC 12,989 and *E. coli* MTCC 40 were used as a control.

Bacterial susceptibility to nanoparticles

E. coli and *S. aureus* were grown in the presence of nanoparticles in liquid medium. The bacteria were grown in 2 ml of the nutrient broth; overnight, via adding NB of the bacterial stock containing 0.12% glucose with and without 1% nanoparticles. The bacteria were aerobically incubated at 37 °C fo 24 h. A high pressure Hg lamp (125 W) equipped with a special UV cut off filter $\lambda > 450$ nm; manufactured by Vilber Lourmat, France offering visible light source was used. It gives an average light intensity equal 60 mW/cm^2 and the working distance was at 30 cm. A continuous cold water ($16 \pm 1\,^{\circ}C$) supply was maintained during the experiment to control the temperature of the reaction mixture. Optical density (OD) measurements were taken at 600 nm to monitor the bacterial concentration with a Hitachi spectrophotometer (type 124).

Isolation of genomic DNA

Genomic DNA was isolated as described previously [34]. Cells from 5 ml overnight culture for each isolate were harvested. Cell pellets were rinsed with 200 μl of NET buffer (0.1 M NaCl, 50 mM EDTA, 10 mM Tris–Cl, pH 8.0) and re-suspended in 200 μl of GET buffer (50 mM glucose,10 mM EDTA, 25 mM Tris–Cl, pH 8.0). 0.001 μg of lysozyme was added and the mixture was incubated at 37 °C for 3 h. Twenty microliters of 10 mg/ml proteinase K was then added and the mixture was incubated at 37 °C for 1 h. One hundred microliters 10% SDS was then added, and the mixture was incubated at 37 °C for 1 h. The mixture was extracted several times with phenol:chloroform:isoamyl alcohol (24:24:1, v/v) until the interface was clear. DNA was precipitated by adding 1/25 volumes of 5 M NaCl and 2.5 volumes of 95% chilled ethanol. The precipitated DNA was rinsed with 1 ml of ice cold 70% ethanol,

air dried, and re-suspended in 30 μl of sterilized distilled water. Selection of primers (In-vitro Gen, Paisley, UK) RAPD was performed as described before [35] with slight modification. PCR reactions were carried out in 25 μl volumes containing 25 ng of total genomic DNA, 10 pmol primer, 200 μM dNTP, 2 mM $MgCl_2$, 1× PCR buffer and 2 units ampli Taq polymerase (RTS *Taq* DNA polymerase). Five random oligonucleotide primers OPA9, OPB7, OPB17, and OPC13and OPE19 were used in the experiment. Premiers were synthesized at Operon technologies, Alameda, USA (Table – see Supporting information). Amplification was performed in PerkinElmer 9600 thermal cycler (Foster City, USA) with the following temperature profile: 94 °C for 5 min followed by 40 cycles of 94 °C for 1 min, 36 °C for 1 min, and extension at 72 °C for 90 s The final extension step was carried out at 72 °C for 5 min. The list of oligonucleotide is given in Supporting information. The PCR products were separated on 1.4% (RAPD) agarose gel in 1× TAE buffer containing 0.1 μg/l of ethiduim bromide for about 2 h at 80 V. Gel was photographed under UV light with Tracktel GDS-2 gel documentation system.

Results and discussion

XRD investigation

The results of XRD analysis of synthesized titania nanopowders derived from polyethylene glycol and polyvinyl alcohol as hybrid polymers (Tev) together with those incorporated with Ag ions ($TevAg_2$-inset)- Fig. 1, confirm the findings of anatase (JCPDS 21-1272) as a major phase and rutile (JCPDS 21-1276) as a minor one. Incorporation of Ag at a loading of 2% decreases the ratio of anatase to 90% in $TevAg_2$. Very small line at $2\theta = 32°$ was also depicted in this sample and ascribed to Ag_2O [36]. Incorporating SWCNT at a loading of 20% relative to titania; synthesized via hybrid polymers, (Tev–SWCNT) did not change the Tev structure but only affected the anatase 1 0 1 phase that exhibited a decrease in intensity and broadness only in $TevAg_2$–SWCNT**.** This might be correlated to superimposing the anatase (1 0 1) peak over that of the CNT (0 0 2) one; assigned to graphitic basal plane reflection of CNTs. The change in the TiO_2 peak shape at 25.5° following MWCNT(Ag) incorporation for rest of samples only showed a lower decrease in intensity relative to Tev–SWCNT. This proposes that a chemical interaction could have occurred between OH groups of TiO_2 and COOH groups exposed on the SWCNT(MWCNT) surfaces. On the other hand, the diffraction pattern of $TevAg_6$–SWCNT indicates characteristic peaks at $2\theta = 38°$ (1 1 1), 44° (2 0 0) and 64.4° (2 2 0) correlated to the standard peaks of Ag° nanoparticles of face centered cubic (fcc) structure (JCPDS, File No. 4-0783) together with the tiny one depicted previously for Ag_2O at $2\theta = 32°$. The relative increase in line-broadening (FWHM) of the TiO_2 peaks in TevAg2–SWCNT than in TevAg2–MWCNT confirms the decrease in crystallites size of the former comparatively probably due to the strong interaction between TiO_2 with SWCNT rather than with MWCNT. The $TevAg_2$–MWCNT sample also motivates the appearance of rutile peaks; never existed in Tev–SWCNT, and Ag° nanoparticles correspond to the 1 1 1 plane. This sample also shows peaks ascribed to Ag_2O correlated to 2 0 0 and 2 2 0 phases together with the previously mentioned peak ascribed to same species at $2\theta = 32.0°$ due to the 1 1 1 site. Retaining TiO_2 structure following SWCNT(MWCNT) and Ag incorporations reflect the intactness of the TiO_2 structure.

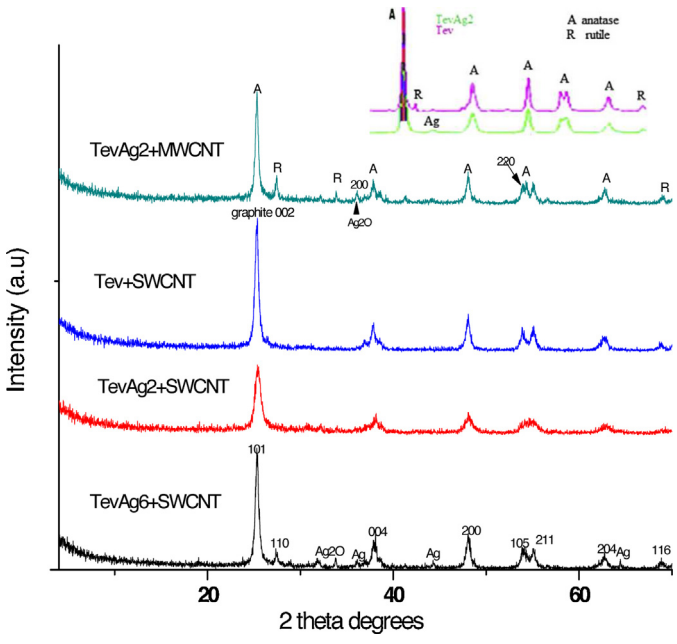

Fig. 1. XRD patterns of TNT–SWCNT, $TevAg_2$–SWCNT, $TevAg_2$–MWCNT and $TevAg_6$–SWCNT.

Surface and morphological properties

The N_2 adsorption–desorption isotherms of pure Tev–SWCNT and Ag containing nanocomposites are shown in Fig. 2. All the samples show similar N_2 adsorption–desorption isotherms. According to IUPAC, the adsorption isotherm belongs to type II, while the desorption isotherm belongs to type IV. Therefore, it can be concluded that the particle size of the prepared samples was mainly distributed in the mesopores range. A clear hysteresis loop at high relative pressure is observed, which is related to the capillary condensation associated with large pore channels. Moreover, the observed hysteresis loops of the samples approach $P/P_o = 1$, suggesting the presence of macropores (>50 nm) [32]. However, the pore size distribution did not show macropores proposing that it can be formed via aggregations of the titanate nanostructures with itself as well as with CNTs. Compared with the as-prepared Tev–SWCNT, the hysteresis loop of the $TevAg_2$–SWCNT sample shows a wider relative pressure range ($P/P_o = 0.4$ –1.0) and larger hysteresis area proposing that Ag nanoparticles stimulate the evolution of microporosities following incorporation as well as giving a hint on the localization of Ag nanoparticles in micropores. This is confirmed from increasing the surface area and decreasing the pore volume values of $TevAg_2$–SWCNT (97.5 m^2/g, 0.132 cc/g) compared with that of Ag free one (86.2 m^2/g, 0.152 cc/g). These later values are diminished in case of $TevAg_6$–SWCNT (81.0 m^2/g, 0.12 cc/g), proposing that the deposition of Ag nanoparticles were deep inside the TiO_2 pores. The pore size distribution of the Tev–SWCNT sample was approximately in the 1.0–4.0 nm range whereas it was narrowed for Ag containing composites to be in the 1.4–3.0 nm range. This proposes that Ag nanoparticles were mainly deposited in the pores around 1 nm i.e., Ag nanoparticles deposited in micropore type of pores. The specific surface area of $TevAg_2$–MWCNT (79.5 m^2/g) indicated a lower value compared with that of $TevAg_2$–SWCNT (97.5 m^2/g) suggesting that MWCNTs are subjected to TiO_2 pores rather than with SWCNTs. The isotherm of the $TevAg_6$–SWCNT sample is somehow typical to type III however the *c* value of this sample was 25 determining strictly that it belongs to type II, as mentioned before. It also shows narrowing the pore size distribution to be mainly around 2 nm; lower limit of mesopores, where it was at 2 and 3 nm for $TevAg_2$–SWCNT.

Fig. 3 shows the TEM images of Ag free as well as Ag containing Tev–SWCNT(MWCNT) composites prepared from the hydrothermal-deposition method and calcined at 400 °C. The image of

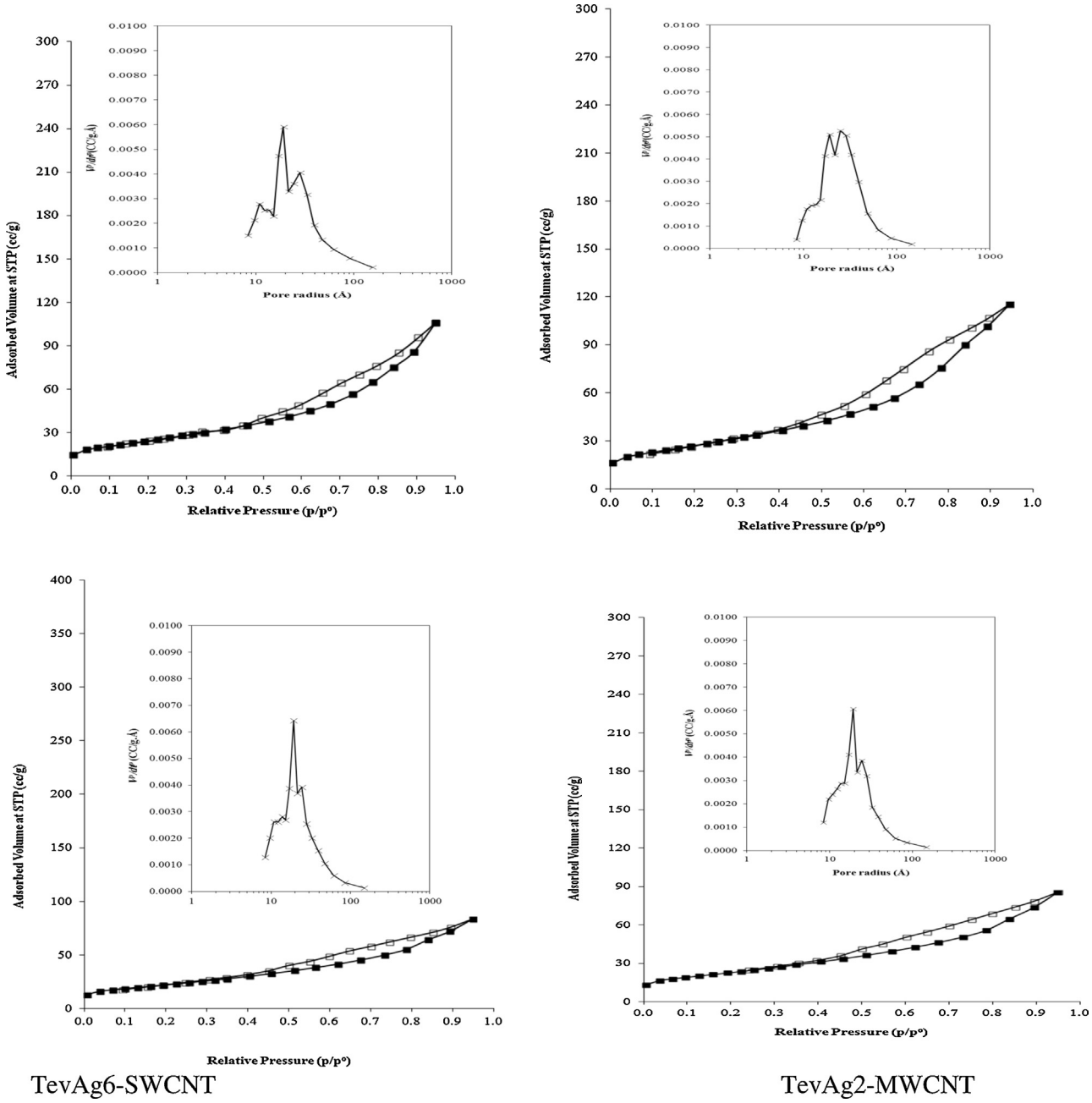

Fig. 2. Adsorption–desorption isotherms of TNT–SWCNT, TevAg$_2$–SWCNT, TevAg$_2$-MWCNT and TevAg$_6$–SWCNT together with their corresponding pore size distributions as insets.

Tev–SWCNT confirmed the existence of TiO_2 nanoparticles coating and covering some parts of CNT surfaces. The diameter of the CNTs was 12–25 nm where the thickness of the TiO_2 nanoparticles was estimated to be in the 7–18 nm range. The insets show the corresponding selected area electron diffraction (SAED) patterns. It shows that diffraction spots of the CNT were overlaid with the diffraction rings of TiO_2 nanoparticles appearing in polycrystalline phases. The selected area electron diffraction patterns show that the circular rings correspond to the planes of CNT (0 0 2), anatase (1 0 1), (0 0 4), (2 0 0), (1 0 5) and rutile (1 1 0) phases from inner to outer rings. This observation is consistent with the wide angle XRD results presented earlier (Fig. 1). The existence of elements Ti, O, C and Ag was detected by EDX analysis (not shown) and confirmed approximately the percentages intentionally prepared. The TEM image of the calcined TevAg$_2$–SWCNT confirmed the presence of anchored crystalline TiO_2(Ag) nanoparticles via uniform coverage of the CNT surfaces. The image shows that the CNT and TiO_2 in the composites indicate an average diameter equal 10 and 12 nm, respectively whereas it decreases to 5 nm for Ag nanoparticles. It can be seen that Ag nanoparticles were well encapsulated inside TiO_2 as a core–shell structure, based on the synthesized procedure, since no Ag nanoparticles were identified with its own in the micrograph as depicted from EDX. The above TEM image confirmed the intactness of the CNT tubular structure with TiO_2(Ag) after calcination. Accordingly, the exhibited decrease in CNT thickness for Ag incorporated composite compared to Ag free one could be a consequence of decreasing both carboxy and hydroxyl groups on sides of CNT surfaces due to TiO_2(Ag) incorporation. In TevAg$_6$–SWCNT and TevAg$_2$–MWCNT samples, it was hard defining the CNT as was in the previous samples

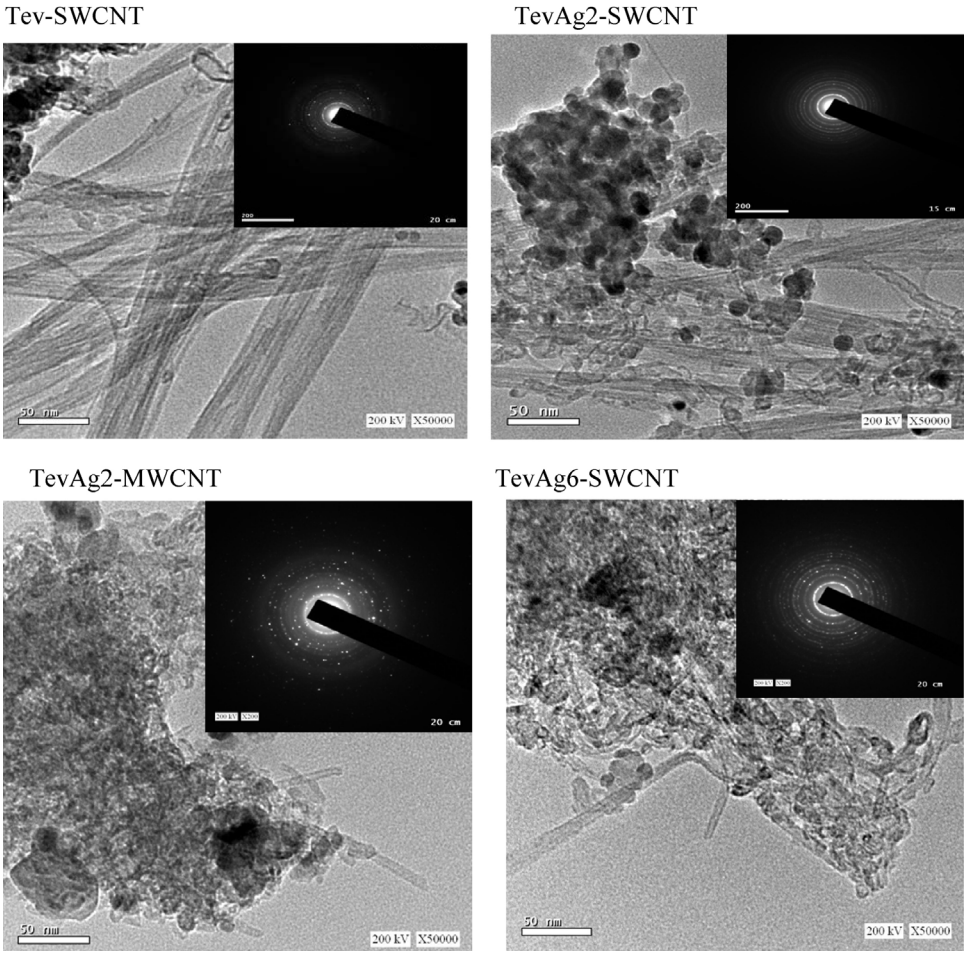

Fig. 3. HR-TEM image TNT–SWCNT, $TevAg_2$–SWCNT, $TevAg_2$–MWCNT and $TevAg_6$–SWCNT together with the corresponding SAED as insets.

declaring more interaction of TiO_2(Ag) with CNTs. Specifically, these later samples showed a significant decrease in CNT thickness; via displaying an outside diameter of ~8 nm, and breaking into shorter tubes. These samples show lower average diameters for TiO_2 (7 nm) and Ag (3 nm) nanoparticles compared to the other samples. This indeed elaborates the extreme interaction between TiO_2 containing Ag nanoparticles and SWCNT/MWCNT structures.

Raman spectroscopy

The Raman spectra of Ag loaded Tev–CNT as well as Ag free nanocomposite samples are shown in Fig. 4. The Raman spectrum of Tev–SWCNT depicted prominent bands for the TiO_2, via exposing bands at 150 cm^{-1} (very strong, E_g), 392 cm^{-1} (B_{1g}), 515 cm^{-1} (A_{1g}) and 634 cm^{-1} (E_g) due to anatase as well as the 260 cm^{-1} (A_{1g}) band ascribed to rutile [38]. This confirms that the synthesized TiO_2 is composed of a mixture of anatase and rutile where anatase phase was being dominant, as earlier confirmed by XRD results. This spectrum also indicates a band at 1582 cm^{-1} indicative of the G band (Raman-allowed E_{2g} mode) characterizing the crystalline nature of the CNTs together with a band at 1332 cm^{-1} (D band, assigned to A_{1g} phonon mode) that measures the distortions on the CNT structures [39]. All the bands correlated to TiO_2 functional groups were decreased in intensity in $TevAg_2$–MWCNT whereas that at 1582 cm^{-1} of CNT showed an enhancement. This indicates that the extent of sp^2 hybridized carbon was more aligned following Ag incorporation. On the other hand, this reflects the extent of the interaction exhibited between Ag

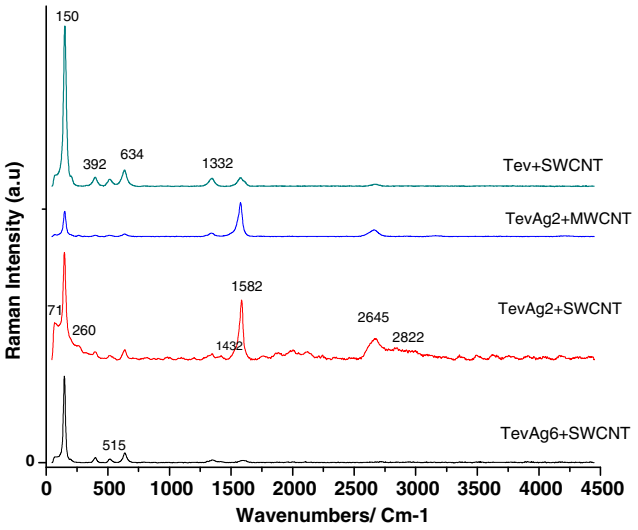

Fig. 4. Raman spectra of TNT–SWCNT, $TevAg_2$–SWCNT, $TevAg_2$–MWCNT and $TevAg_6$–SWCNT.

nanoparticles within TiO_2 structures rather than with CNT; as devoted from declining the bands related to TiO_2. This was also emphasized from TEM results. Comparing the Raman spectrum of $TevAg_2$–SWCNT relative to that of $TevAg_2$–MWCNT elaborates different interaction themes depending on the CNTs type. In conformity, $TevAg_2$–SWCNT that retains considerable fraction of

the 1582 cm^{-1} band as well as the 2645 cm^{-1} one; an overtone mode of the D band, indicates that SWCNT is the least affected and distorted either by incorporating Ag or TiO_2. The presence of small broad band at 1432 cm^{-1} in the later sample dictates also the presence of amorphous carbon. It is worth noting that the synergistic effect occurs only if the TiO_2 is chemically attached to the carbon nanotubes. The main three bands (392, 515, 634 cm^{-1}) in the Raman spectrum representative of anatase TiO_2 are narrowed and followed the order: $TevAg_2$–SWCNT > $TevAg_6$–SWCNT > $TevAg_2$–MWCNT as compared to the Tev–SWCNT composite sample. On the other hand, the broadness of the Raman band at 1332 cm^{-1} in $TevAg_2$–MWCNT and $TevAg_6$–SWCNT as compared to Tev–SWCNT may be due to the strain gradients originating from interface integration of TiO_2 and CNTs and to the varied adherence of TiO_2 particles to SWCNT(MWCNT) surfaces; as also confirmed via TEM observation. In case of $TevAg_6$–SWCNT, the hardly present CNT bands compared with those of TiO_2 ones dictates that the excess Ag nanoparticles corresponded to the former structure than to the latter one.

FTIR spectroscopy

The surface groups of TiO_2 are helpful to form chemical bonding with those oxide groups exposed on CNTs. The FTIR spectrum of Tev–SWCNT (Fig. 5) indicates bands at 3423, 1627, 1384, 722 and 530 cm^{-1}. The strong and broad characteristic band occurred in the 3100–3700 cm^{-1} (3423 cm^{-1}) range constitutes with the one at 1627 cm^{-1} [40] the presence of O—H stretching vibrations in C—OH groups and the OH bending vibration of chemisorbed or physisorbed H_2O molecule on the photocatalyst surface, respectively. The obtained IR prominent band at 1384 cm^{-1} is mostly attributed to the aliphatic stretching frequencies of CH_x groups [41]. Furthermore, the broad band at 722 cm^{-1} could be assigned to the combination effects of both Ti—O and Ti—O—C bands in CNT/TiO_2 nanocomposite [40]. Whereas that at 530 cm^{-1} characterizes Ti—O of anatase structure. Insertion of Ag nanoparticles causes some changes such as shifting the 722 cm^{-1} band into 630 cm^{-1}; as in $TevAg_6$–SWCNT, and to 619 cm^{-1}; as in $TevAg_2$–SWCNT, together with evoking a new band at 1126 cm^{-1} ascribed to the presence of an ester localized group. Only in $TevAg_6$–SWCNT, a small broad band at 1725 cm^{-1} due to C=O stretching vibrations in carboxyl groups was obtained. This indicates the expansion of carboxylation on the surfaces of functionalized SWCNTs. The absence of bands related to vibration of C=C (1530–1560 cm^{-1}) in favor of that at 1725 cm^{-1} is a proof of CNT oxidation and its existence even following the TiO_2(Ag) incorporation. This verifies that the oxide groups are not totally used up even following incorporation with TiO_2(Ag). It seems that the strong interaction devoted between Ag and TiO_2, confirmed via the noticed shift, gives a space to expose oxide groups on CNT surfaces. This proves that the chemical oxidation of SWCNTs via oxygen containing surface groups is well achieved and indeed takes part in adherence with TiO_2. The disappearance of the 530 cm^{-1} band following Ag incorporation probably depicts the interaction of Ag with Ti—O bonds; as proposed previously using TEM–EDX and Raman. The spectrum of $TevAg_2$–MWCNT presented the same bands as those shown in all Ag containing samples but with a decrease in intensity. This suggests that the surface of TiO_2 has probably been partially covered by MWCNTs. This admits that the surface groups of TiO_2 form stronger chemical bonding with MWCNTs rather than with SWCNTs. Simultaneously, the peak at 3423 cm^{-1} showed a marked decrease in intensity indicating that the OH groups of TiO_2 had been partially decomposed after the reaction with Ag^+/Ag° species and rather proposes an interaction of Ag with O-atoms.

Photoluminescence spectroscopy

Notably, the positive synergy effects of CNTs and TiO_2 depend on both the CNT loading amount and the state of interfacial contacts. Curves of Tev–SWCNT(MWCNT) containing Ag nanoparticles (Fig. 6) showed a greatly enhanced photoemission spectra of ratio comprised of 6–10 compared to Ag free Tev–SWCNT sample. Increasing PL intensities of Ag containing composites can be accounted for the higher rate of recombination of electrons and holes. Therefore, the strong photoluminescence of Ag containing composites is due to the intensive coupling between Tev and localized surface plasmon of Ag nanoparticles [42]. The room-temperature photoluminescence spectra of Tev–SWCNT synthesized by hydrothermal method showed an emission peak centered at 361 nm due to fine crystallized TiO_2 together with the well-known broader emission peak situated at 335 nm attributed to CNTs. These ultraviolet emission intensity peaks decreased in intensity in all Ag containing composites probably due to low crystalline quality. A dramatic enhancement in photoluminescence intensity of $TevAg_2$–MWCNT compared with other Ag containing composites was demonstrated. This verified that surface and/or localized surface plasmons of various Ag metals in MWCNT indeed exceeded those on SWCNT. Indeed, this measures the rate of recombination of electrons and holes in this sample comparatively.

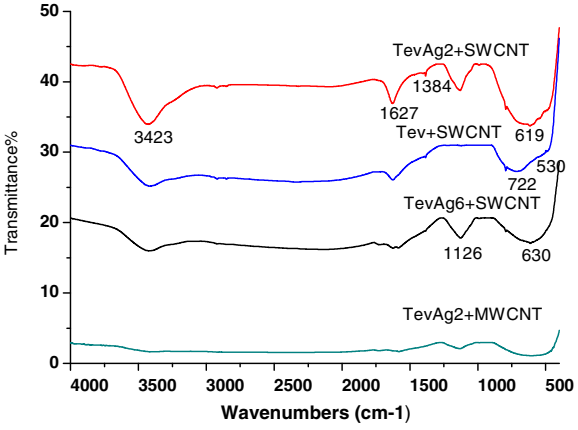

Fig. 5. FTIR spectra of TNT–SWCNT, $TevAg_2$–SWCNT, $TevAg_2$–MWCNT and $TevAg_6$–SWCNT.

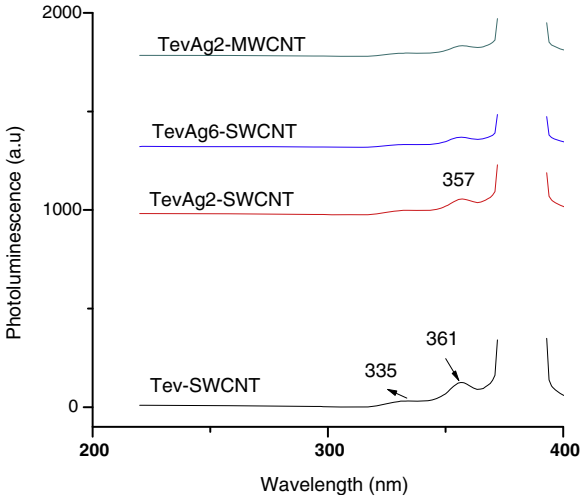

Fig. 6. PL spectra of TNT–SWCNT, $TevAg_2$–SWCNT, $TevAg_2$–MWCNT and $TevAg_6$–SWCNT.

Although the silver content on the surface of $TevAg_6$–SWCNT was optimum, it efficiently traps the photoinduced electrons and acts as a charge separator, thereby increasing the life time of electron and holes compared to $TevAg_2$–MWCNT. The PL intensity of $TevAg_2$–SWCNT was the lowest between all Ag containing composites. This indicates that the CNT materials can act as electron reservoirs to trap or shuttle the photogenerated electrons from semiconductors [43] based on its type [SWCNT(MWCNT)], nature of CNT interaction with TiO_2 and loading of Ag nanoparticles. However, notably SWCNT is capable to exhibit its superior electron conductivity for trapping the photogenerated electrons to prolong the lifetime of charge carriers as compared to MWCNT.

Optical properties

In order to elucidate the optical response and to determine the band gaps of the nanocomposite samples, UV–visible diffuse reflectance spectroscopy (UV–vis DRS) was carried out, and the results are depicted in Fig. 7. The spectral absorbance was measured in the wavelength range of 200–800 nm. Although the spectral shapes are generally same, there are prominent differences in the absorption edges. The Tev–SWCNT composite exhibits a band at 286 nm together with a broad one at 353 nm. Generally, anatase-type TiO_2 has a strong absorption edge below ca. 350 nm whereas that of CNT exhibits a band at ca. 280 nm due to π–π^* transition of the C—C aromatic ring. In comparison, the absorption edge of $TevAg_2$–SWCNT displays the similar absorption edge of Tev–SWCNT, but an apparent enhancement of absorption throughout the visible-light region is observed with diminishing that at 280 nm. This probably correlated to the exhibited dispersion and interaction of TiO_2(Ag) with CNT; as evidenced previously using Raman and IR spectroscopies. Absorption changes in the UV–vis spectra obviously highlight the enhancement of visible-light absorption upon increasing the Ag content into 6%. The adsorption intensity of the $TevAg_2$–MWCNT sample was extremely enhanced compared with $TevAg_2$–SWCNT owing to the good dispersion as well as the strong interaction of Ag(TiO_2) with MWCNT exceeding that with SWCNT; as denoted previously using XRD, Raman and IR techniques. This result suggests that the TiO_2/MWCNT nanocomposites combined the features of MWCNTs and TiO_2 together, which may modify the process of the electron/hole pair formation under visible light irradiation [44]. In addition, the $TevAg_2$–MWCNT sample exhibits a band at 216 nm never seen in nanocomposites involved SWNCT probably correlated to the exhibited strong interaction between MWCNTs and TiO_2. Interestingly, $TevAg_2$–MWCNT exhibited the strongest absorption among those nanostructured carbon/TiO_2 composites; as confirmed from both shifting the band at 352–357 nm as well as enhancing the broadness that extends to 800 nm, proposing an intense electronic interaction at the interface of TiO_2/MWCNT. Moreover, the MWCNTs/TiO_2(Ag) composite exhibited enhanced visible-light-absorption; as well as highest emission as confirmed from PL measurements, exceeding those of free Ag and Ag containing SWCNT/TiO_2. This can be recognized to the increased electronic density and the strong adherence between MWCNT and TiO_2 exceeding those between SWCNT and TiO_2. This same sample indicates a band at 260 nm probably due to CNT deformation. This indeed was seen in TEM results via shortening and narrowing CNT segments. All Ag containing composites showed a surface plasmon resonance band at 440 nm originated from the collective oscillations of the electrons at the surface of the nanoparticles. It is obvious that the resonance bands are not broad reflecting the narrow size distribution of Ag nanoparticles; as shown in TEM images.

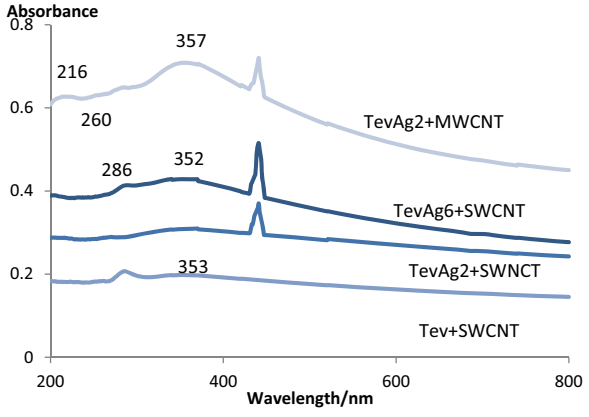

Fig. 7. UV–vis absorption spectra of TNT–SWCNT, $TevAg_2$–SWCNT, $TevAg_2$–MWCNT and $TevAg_6$–SWCNT.

In order to determine E_g, we have analyzed the measured absorption spectra of the studied nanocomposites, by calculating the absorption edge based on the following approximation [45]: $\alpha(h\nu) \propto (h\nu - E_g)n/2$ where, the relationship between the absorption coefficient α and the incident photon energy $h\nu$ near the band edge is estimated (Fig. 8). The values of optical transition obtained by extrapolating the straight line portion to energy axis at zero absorption coefficients give the direct optical band gaps. In particular, we found that E_g decreases in the following sequence: Tev–SWCNT (2.6) > $TevAg_2$ – SWCNT (2.25) > $TevAg_6$ – SWCNT (1.9) = $TevAg_2$ – MWCNT (**1.75**). These results indicate the capability of the later samples for capturing visible light, comparatively. Smaller band gap values were clearly observed for $TevAg_6$–SWCNT and $TevAg_2$–MWCNT composites. This proposes an intense electronic interaction between Ag(Tev) and SWCNT(MWCNT). Additionally, decreasing the E_g for $TevAg_6$–SWCNT and $TevAg_2$–MWCNT; those showed the highest absorption, proposing that CNT acted as a photosensitizer when coupled with TiO_2, then it can be excited to inject electrons into the conduction band of TiO_2. It seems that the incorporation of MWCNTs stimulate the absorption to be higher than TiO_2 in the visible region, as they act as good electron acceptors capable of capturing electrons from light irradiation [46]. This exhibits that $TevAg_6$–SWCNT and $TevAg_2$–MWCNT composites will be more excellently photoactive than rest of the samples based on dispersion of CNTs in TiO_2.

Visible light irradiation of RhB

The normalized temporal concentration changes (C/C_o) of RhB during the photodegradation; proportional to the normalized maximum absorbance (A/A_o), are derived from the changes in RhB's absorption profile (λ = 540 nm) at a given time interval (Fig. 9). RhB degradation in the absence of photocatalyst is negligible under visible light irradiations because electron recombination between the injected electron and the excited dye*+ is fast in the photosensitization process. Under dark conditions, the RhB dye showing equilibrium adsorption comprised respectively of 6, 8, 9 and 12% for Tev–SWCNT, $TevAg_2$–SWCNT, $TevAg_2$–MWCNT and $TevAg_6$–SWCNT after 60 min time. The removal efficiency of the pollutant RhB dye was studied by visible light-driven photocatalytic degradation. It is clearly shown in Fig. 10 that, Tev–SWCNT, the two-phase composite revealed around 20% degradation towards RhB under visible light illumination in 80 min. However, the presence of Ag in the composite causes an improved photocatalytic activity when the amount was increased from 2 to 6 wt%. Thus, in the three composite photocatalysts $TevAg_2$–SWCNT, $TevAg_2$–MWCNT and $TevAg_6$–SWCNT, a gradual increase in the degradation efficiency from 40%, 59% and

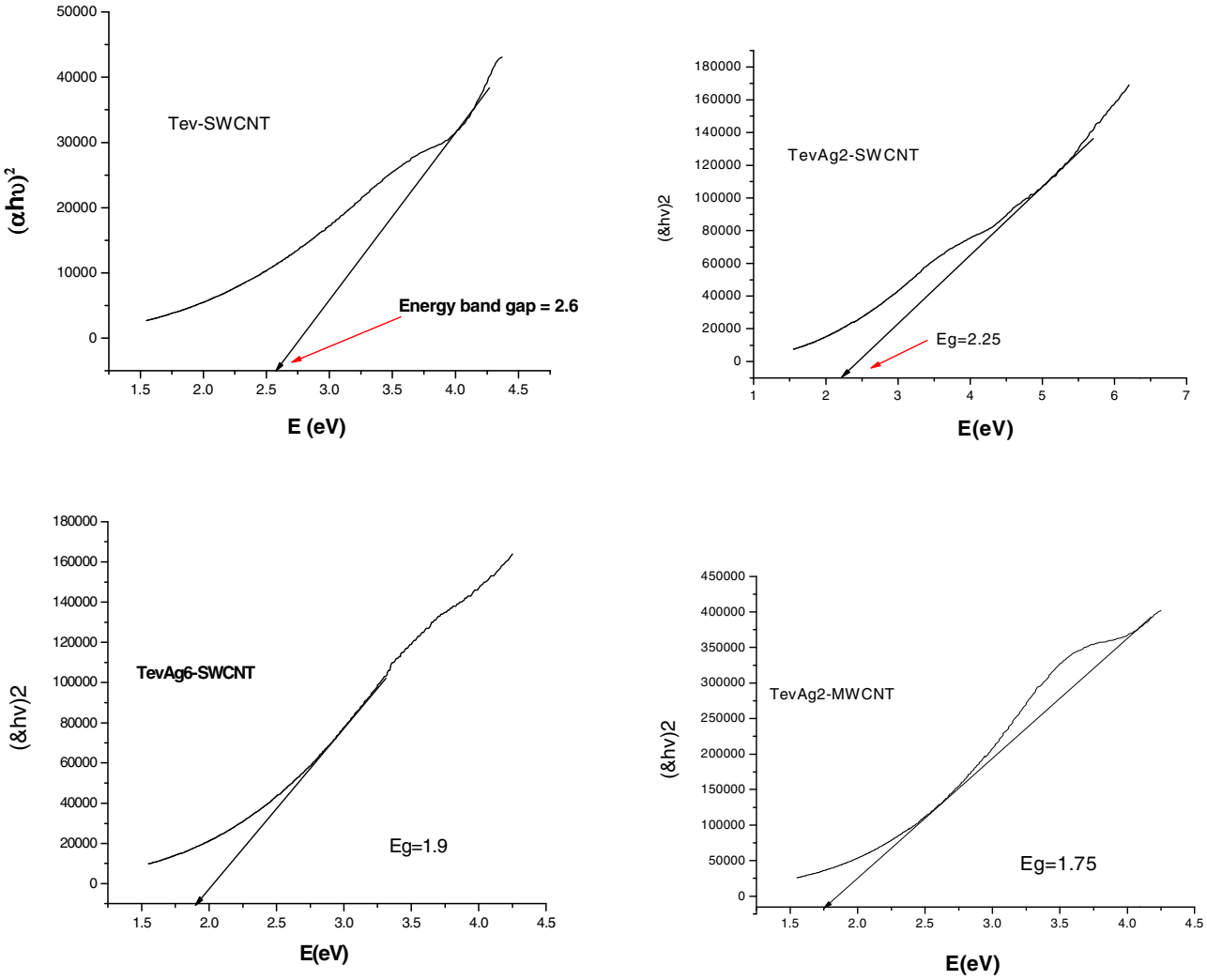

Fig. 8. E_g values of TNT–SWCNT, $TevAg_2$–SWCNT, $TevAg_2$–MWCNT and $TevAg_6$–SWCNT.

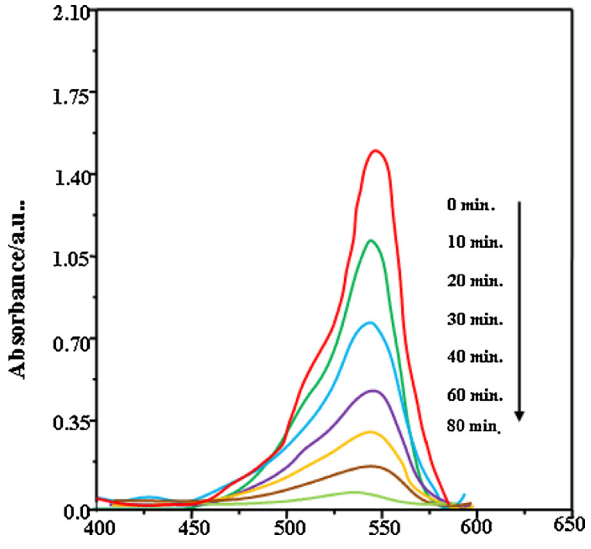

Fig. 9. Absorption spectra of RhB (λ_{max} = 540 nm) under visible light irradiation on $TevAg_6$–SWCNT as a function of time.

100%, respectively was established. To be sure that we are dealing with photodegradation process and not a decolorization, we performed TOC measurements. The normalized TOC was found to depend on the illumination time for the RB degradation assisted by $TevAg_6$–SWCNT. After 80 min illumination time, no RB could be detected by UV–vis spectroscopy (as configured before in Fig. 9) and the carbon concentration decreased by about 95% of the initial concentration (not shown). Further irradiation for 20 min reduces TOC into zero. This demonstrates that no RB is left in the reaction mixture, however, minute amounts of organic carbon could be left after 80 min, most likely aldehydes/carboxylic acids [47]. In order to reveal the active species responsible for the enhanced photocatalytic activity, three different chemicals *p*-benzoquinone (BZQ, an $O_2^{\bullet-}$ radical scavenger), disodiumethylenediaminetetraacetic acid (Na_2–EDTA, a hole scavenger) and isopropanol (an $^{\bullet}OH$ radical scavenger) were utilized as scavengers for holes and radicals trapping experiments. As shown in Fig. 11, when 5 mM Na_2–EDTA was added, a negligible effect on the degradation of RhB was observed where almost 90% RhB was degraded over the $TevAg_6$–SWCNT composite. A notable inhibitory effect on the degradation activity over the latter photocatalyst was observed in case of BZQ (5 mM) and isopropanol (5 mM), in which less than 30% and 20% RhB were respectively degraded. Increasing the latter reactive radical scavengers concentration into 10 mM during irradiation caused even worse efficiencies reaching 2–3% degradation. Thus, it

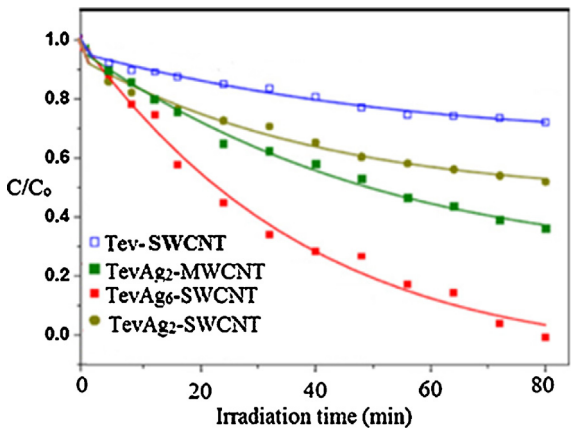

Fig. 10. Photocatalytic degradation of RhB by TNT–SWCNT, $TevAg_2$–SWCNT, $TevAg_2$–MWCNT and $TevAg_6$–SWCNT photocatalysts under visible light irradiation: reaction conditions: (filter $\lambda > 450$ nm, catalyst weight 30 mg, dye conc. 20 ppm).

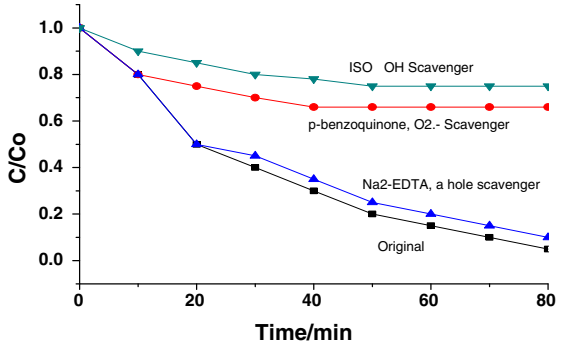

Fig. 11. Effect of reactive scavengers on the activity of the $TevAg_6$–SWCNT photocatalyst toward RhB degradation performed under visible light irradiation in a way for evaluating the degradation mechanism.

is suggested from these trapping experiments that active photoinduced $^{\bullet}OH$ and $O_2^{\bullet-}$ radicals rather than holes are dominant species responsible for the high efficient photocatalytic activity. The reason for higher activity of $TevAg_6$–SWCNT can be explained by considering the Ag nanoparticles to form locally Schottky junctions with a higher potential gradient at the Ag/TiO_2 interface [17,18] based on exceeding the work function of the Ag than TiO_2 [36]. The formation of the latter junction has been comprehended via formation of the core–shell of Ag/TiO_2 as confirmed by TEM observations. It is also obvious that Ag nanoparticles have strong influence on the photoactivity of $MWCNT/TiO_2$ composite that showed remarkable adsorption equilibrium (60 min) reaching 12% in $TeVAg_6$–SWCNT. Indeed, this favorable adsorption is evoked by CNT that is accomplished via $\pi-\pi$ stacking between RhB and aromatic moieties of the SWCNTs [45]. Although the surface area and pore volume of $TevAg_6$–SWCNT are slightly lower than those of MWCNT–TiO_2 and $TevAg_2$–SWCNT, it exhibits higher photocatalytic activity (100% degradation in less than 80 min under visible light illumination) comparatively. Considering the work function of MWCNT (4.95 eV) and TiO_2 (4.4 eV), excited RhB can efficiently inject electrons into the TiO_2 conduction band, which can further move to MWCNT due to lowering the work function of TiO_2 than MWCNT. The photo excited electrons of TiO_2 conduction band can be readily scavenged through multi-walled carbon nanotubes when they are coupled (Ti—O—C). Moreover, carbon nanotubes can modify the electronic structure of TiO_2 by narrowing the band-gap thus, rendering TiO_2 more sensitive to the visible light. It is commonly acknowledged that the noble metal, Ag, acts as a sink for photoinduced charge carriers and promotes interfacial charge transfer processes. Accordingly, the photogenerated electrons in TiO_2 following the visible irradiation move to the Ag metal as well as CNTs and thus the electrons on Ag metal participate in catalytic reactions. However, increasing the percentages of Ag_2O on the surface of $TevAg_2$–MWCNT; that showed lower activity than $TevAg_6$–SWCNT, nullify its role in the degradation process. Based on the studies of reactive species performed under visible light illumination, photo-excited electrons from the dispersed Ag/TiO_2 are injected into CNTs channels affirmed through the combination of TiO_2–CNT i.e., the formation of the Ti—O—C bonds. On the other hand, the existed holes can react with surface hydroxyl ions or water molecules to produce hydroxyl radicals ($OH^{\bullet}$). While electrons trapped by the Ag can react with adsorbed molecular oxygen and/or with C=O yielding superoxide radicals ($O_2^{\bullet}$).

The reaction rates of the catalysts indicate a decrease in the following order: $TevAg_6$–SWCNT > $TevAg_2$ – MWCNT > $TevAg_2$ – SWCNT > Tev–SWCNT. There is a pronounced dependence of the activity on the dispersion of Ag moieties; i.e., the activity is increased with decreasing Ag particle sizes to 3 nm as depicted from the TEM results of $TevAg_6$–SWCNT. PL spectra show that although the silver content on the surface of $TevAg_6$–SWCNT was optimum, it efficiently traps the photoinduced electrons and acts as a charge separator, thereby increasing the life time of electron and holes compared to $TevAg_2$–MWCNT. Although $TevAg_6$–SWCNT presented a slight increase in E_g (1.9 eV) than $TevAg_2$–MWCNT (1.75 eV), the former presented higher activity. This indeed is in part due to exposing rutile TiO_2 in $TevAg_2$–MWCNT; of lower absorptivity and lower photosensitivity than the corresponding anatase, as well as to the exhibited MWCNT severs deformation exceeded that of SWCNT, which might limit the passage of electrons in a normal way. In addition, increasing the activity of $TevAg_6$–SWCNT might also be correlated to the presence of C=O localized groups on its surface never seen on other samples. One of the economic vital factors in catalytic processes is the stability of the catalyst. This factor was measured by completing several consecutive experiments with the $TevAg_6$–SWCNT photocatalyst under uniform operating conditions (Fig. S1). The catalyst presented potential recycling ability comprising of 95% after 240 min reaction time.

Table 1
Zone of inhibitions of different nanoparticle samples against *S. aureus* and *E. coli*.

Sample Name	Zone of inhibition mm (S. aureus) 100 μg/ml	Zone of inhibition mm (E. coli) 100 μg/ml
$TevAg_2$ + MWCNT	23	25
Tev + SWCNT	9	No result
$TevAg_6$ + SWCNT	30	45
$TevAg_2$ + SWCNT	22	25
Tev	2	No result
$TevAg_2$	7	5
$TevAg_6$	12	15

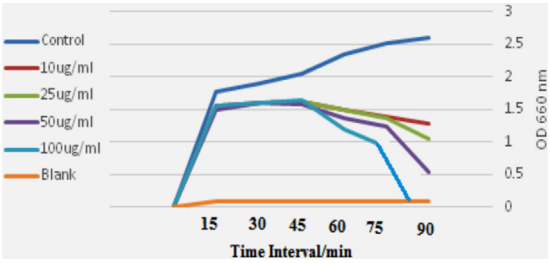

Fig. 12. Effect of visible light irradiation of $TevAg_6$–SWCNT on the growth of *E. coli*.

Antibacterial activity of nanoparticles under dark conditions against pathogenic gram-negative bacteria E. coli *and gram-positive bacteria* S. aureus

The antibacterial activity of silver nanoparticles was investigated against pathogenic gram-negative strain (*E. coli*) and gram-positive strain *S. aureus* using well diffusion technique (see Supporting information, Fig. S2). Negative control was maintained in which no zone of inhibition was observed. Positive control using antibiotic test disk was also obtained (Fig. S3). The diameter of inhibition zones around each well in presence of nanosamples is represented in Table 1. The highest antimicrobial activity observed against *E. coli* was 40 mm for $TevAg_6$–SWCNT, and the least was 25 mm for $TevAg_2$–SWCNT(MWCNT) samples. The positive control highest activity was 30 mm and the least was 10 mm. On the other hand, the highest antimicrobial activity observed against *S. aureus* was 30 for $TevAg_6$–SWCNT and the least was 22 and 23 mm for $TevAg_2$–SWCNT and $TevAg_2$–MWCNT, respectively. Conversely, it seems that bacteria resist the influence of Ag free Tev sample while moderate effects were exhibited in Tev containing Ag nanoparticles especially that at the loading of 6% (Table 1). This indeed reflects that the presence of CNT enhanced the bactericidal performance when added to Tev containing Ag nanoparticles. On the basis of the obtained results, the $TevAg_6$–SWCNT ternary composite was chosen for further investigation.

Bactericidal effect of nanosilver on E. coli *and* S. aureus *in liquid media*

The antibacterial effects of nanocomposites towards *E. coli* and *S. aureus* in liquid media for different time intervals; in the dark, indicated the highly efficient inhibition of *E. coli* and *S. aureus* growth as compared to control groups. For *E. coli* concentration, 100 μg/ml caused 20 times decrease in the optical density of bacterial culture as compared to control experiment, (Fig. S4). The same decrease was also exhibited for *S. aureus* and at the same concentration (Fig. S5). On the other hand, exposure of the $TevAg_6$–SWCNT catalyst to visible light irradiation reduces the inhibition time of *E. coli* from 18 h in the dark (Fig. S4) to only 85 min (Fig. 12). This indeed highlights the photocatalytic action of this material. It seems also that the trend of the curves for the latter sample was almost same in the dark and under irradiation reflecting probably the same mechanism or same exposed species.

Effect of nanoparticles on the bacterial DNA

The effect of nanoparticles; specifically sample $TevAg_6$–SWCNT that gives the maximum inhibition towards both types of bacteria, was conducted by using RAPD PCR. This is the first report to study the effect of nanoparticles on the bacterial DNA; at least to our knowledge on similar samples. In Fig. 13A, using primer OPA-09 and after 14 h of growth with nanoparticles there were 3 new bands at 0.3, 0.6 and 0.8 kbp were not present in the control. On the other hand, the absence of 3 bands at 1, 2 and 2.8 kbp was noticed while after 10 h of growth of *E. coli* with nanoparticles, there was a disappearance of the band at 0.7 kbp. Fig. 13B shows that on using primer OPB-07 and after 14 h of growth, the disappearance of the band at 1 kbp for the *E. coli* growth with nanoparticles was depicted, and there were 3 new bands existing at 0.8, 2 and 1.2 kbp after 10 h of growth. After 6 h of growth there was no difference between bacterial growth with or without nanoparticles. In Fig. 13C, a new band at 1.3 kbp is revealed where the band at 0.8 kbp is missed after 14 h of growth and after 10 h of growth with nanoparticles there was a new band at 0.4 kbp. In Fig. 13D, the absence of the band at 0.8 after 14 h of growth of *E. coli* with nanoparticles was noticed. No significant differences between *E. coli* growth with or without nanoparticles after 6 and 10 h using primer OPC-13 were seen. The effect of nanoparticles on *S. aureus* was also conducted using the same technique RAPD PCR (see Supporting information Fig. S6). These figures reveals the absence of some bands and the evolution of some others accomplishing that mutations have been taken place on the bacterial cell wall.

A comparative study of our silver containing composites with previous work revealed that our synthesized samples have higher antibacterial potency than previously published work [48,49]. In addition, it has been shown that nanosilver affected gram-negative bacteria much more than gram-positive bacteria. This is because the bacterial wall in gram-negative bacteria is thinner than gram-positive bacteria [50]. In addition, the effect of nano silver (NS) particles size was very well correlated with the bactericidal activity i.e., decreasing the particle size of Ag° nanoparticles encapsulated inside TiO_2 into to 3 nm; particularly in $TevAg_6$–SWCNT, was one of the detrimental effects on killing bacteria. This same sample restrictively shows the exposure of C=O and OH groups on the surface of SWCNT; as configured from FTIR results, proposing oxidative damage to bacterial DNA; as mentioned previously [46–48]. However, decreasing the bactericidal efficiency of $TevAg_2$–MWCNT even though it presents Ag°

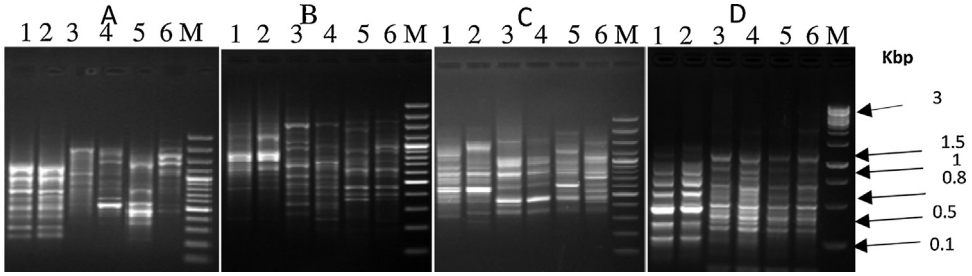

Fig. 13. RAPD PCR profile of *E. coli* by using 10 mer primer lane M: 100 pb plus marker, panel A–D lane 1: bacterial growth after 6 h without nanoparticles, lane 2: bacterial growth after 6 h with nanoparticles, lane 3: bacterial growth after 10 h without nanoparticles, lane 4: bacterial growth after 10 h with nanoparticles, lane 5: bacterial growth after 14 h without nanoparticles, lane 6: bacterial growth after 14 h with nanoparticles.

nanoparticles of 3 nm diameter; as in the latter sample, probably due to lowering of the Ag° concentration and to the deterioration of the MWCNT compared with SWCNT upon incorporation with TiO_2. In addition, although the exhibited interaction between TiO_2 and MWCNT exceeded that with SWCNT; as devoted from XRD, Raman, FTIR and TEM measurements, they almost show ($TevAg_2$–SWCNT and $TevAg_2$–MWCNT) similar antibacterial behavior towards *E. coli* and *S. aureus* strands. This intensifies the importance of the interaction between Ti and C that was attained via exposed surface oxygen irrespective of CNTs type. Accordingly, the TiO_2–CNT heterojunction could minimize recombination of photoinduced electrons and holes; as elaborated via PL and UV-diffuse reflectance measurements, and had a more effective light absorption when Ag nanoparticles are incorporated at a loading of 6%. Appreciable activity was also gained for Ag free Tev–SWCNT photocatalyst specifically towards gram-positive *S. aureus* (Table 1) due to Ti—C and Ti—O—C bonds formed at the heterojunction which is responsible for visible light absorption and photocatalytic oxidation processes. It was proposed that they were efficiently contributed in the charge transfer between the photoexcited MWNTs and TiO_2 and thus reducing the e^-–h^+ recombination process. Accordingly, an increase in the concentration of OH radicals was exhibited and affected bacterial degradation. As a diagnostic tool for OH radical diffusion, a small amount of isopropanol (0.001 ml of 5×10^{-3} M) was added as a scavenging agent while performing the agar well diffusion method to the *E. coli* strand in presence of the $TevAg_6$–SWCNT photocatalyst. The presence of this agent significantly lowered the photocatalytic activity of the composite verifying the lethal effect of OH radicals that induces a decrease in the inhibition zone from 45 to 20 mm. On the other hand, the absorbed oxygen on CNT/TiO_2 interface reacts with electrons to mainly form superoxide radicals ($O_2^{\bullet -}$), which effectively oxidized bacteria as evaluated via using 0.001 mM *p*-benzoquinone radical scavenger. This indeed elaborates the absorption capability of our sample to sunlight. Upon using Na_2–EDTA, as a hole scavenger, no inhibitory effect on the bacterial growth was noticed. Although $TevAg_6$–SWCNT shows higher E_g than $TevAg_2$–MWCNT, the former indicates higher antimicrobial action probably due to increasing the recombination rate of electrons and holes on the latter sample comparatively, as confirmed from PL measurements. On the other hand, the presence of appreciable percentages of Ag_2O in the crystal structure of latter two samples; as devoted from XRD and previous XPS results [17], and their expected diffusion towards the crystal surface of TiO_2, and interacting with bacteria surfaces causing their deactivation must be considered. However, revealing no differences in activity between $TevAg_2$–MWCNT and $TevAg_2$–SWCNT indicate the non influence of Ag_2O species that has been noticed in the former sample but not on the latter. On the basis of the above photocatalytic bactericidal results, it can be suggested that the $TevAg_6$–SWCNT composites have improved activities exceeding Tev, $TevAg_x$ as well as the two phase composites due to synergistic effect of irradiated Tev and Ag° together with high surface area CNTs. In this context, under visible light irradiation, silver can act as electron traps which enhance electron–hole separation in TiO_2. On one hand, a fast electron transfer from Ag° to CNT of high adsorption capacity surfaces may also cause recombination delay and thus electrons are free to react to form radicals that are efficient in the photocatalytic degradation of bacteria.

Although the exact mode of action of AgNPs to bacterial membrane is still not very clear, possible mechanism of action has been suggested according to the morphological and structural changes in the bacterial cells. It is assumed that the high affinity of silver towards sulphur and phosphorus is the key element of the antimicrobial effect. Cysteine is a compound of the bacterial wall. This amino acid posses reactive thiol groups —SH. Silver ions interact with cysteine residues leading to protein inactivation. Apart from sulfur, silver has a high affinity to phosphorus as well as forming complexes with compounds containing these elements. Deposition of silver NPs in the bacterial cell surface can affect cell membrane permeability as well as affect the bacterial cell wall as well. It may lead to disturbances in ions transportation and other substances between bacterial cell and its surrounding [46,47]. The diminished activity of cell membrane sodium/potassium pumps results in water flux into bacteria cell and an enlargement of the cell volume [46,47]. NS can destruct a cell membrane and lead to bacterial cell lysis. Numerous researches support the fact that a considerable target site for nanostructured silver is the genetic material of the bacterium [51]. It was found that DNA loses its replication ability once the bacteria are treated by nanosilver containing composites, and this is indeed associated with nanosilver capacity for binding to phosphorane residues of DNA molecules. Moreover, NS also affect gene expression. In *E. coli*, silver was observed to stop S2 protein expression, a component of 30S ribosomal subunit and its denaturation. At the same time, the expression of genes encoding other proteins and enzymes involved in energy reactions, in that ATP synthesis was stopped [52]. A denaturation of ribosomes leads to the inhibition of protein synthesis [53]. Silver ions can bind to the bases constructing DNA. This interaction with DNA leads to its inability to replicate preventing the bacterial reproduction [53].

Conclusion

It has been shown that the $TevAg_6$–SWCNT photocatalyst, synthesized using deposition–hydrothermal method, has the ability to capture visible light, showed the highest activity towards RhB degradation and as antibacterial agent against *E. coli* and *S. aureus*. The physicochemical properties obtained via using many techniques give a clue regarding the efficacy of Ag containing composites and we can summarize them into: (i) decreasing Ag particles size into lower values as low as 3 nm showed effective inhibition to various strands of bacteria, (ii) the formed Ti—O—C bonds at the heterojunction played a unique role in slowing the e^-h^+ recombination and increasing the rate of $^{\bullet}OH$ and $O_2^{\bullet -}$ radicals responsible for degradation of both organic dyes and bacteria, (iii) Ag free Tev–SWCNT sample presented no response to *E. coli* since it shows more negatively charges on its surface than that of *S. aureus*, thus prohibiting the interaction with negatively charges exposed on TiO_2 as well as on CNT, existed via residual carboxylated moieties, (iv) SWCNT was capable to extend the lifetime of charge carriers as compared to MWCNT, as devoted from PL results.

Acknowledgement

This work was financially supported by the King Abdulaziz City for Science and Technology Research Grants Program # 11-NAN1694-10.

References

[1] E.T. Thostenson, C.Y. Li, T.W. Chou, Nanocomposites in context, Compos. Sci. Technol. 65 (3–4) (2005) 491–516, doi:http://dx.doi.org/10.1016/j.compscitech.2004.11.003.
[2] k.T. Lau, C. Gu, D. Hui, A critical review on nanotube and nanotube/nanoclay related polymer composite materials, Compos. B Eng. 37 (6) (2006) 425–436, doi:http://dx.doi.org/10.1016/j.compositesb.2006.02.020.
[3] A. Fujishima, K. Honda, TiO_2 photoelectrochemistry and photocatalysis, Nature 238 (5358) (1972) 37–38, doi:http://dx.doi.org/10.1038/238037a0. 12635268.
[4] I.K. Konstantinou, T.A. Albanis, TiO_2-assisted photocatalytic degradation of azo dyes and mechanistic investigations, Appl. Catal. B Environ. 49 (1) (2004) 1–14, doi:http://dx.doi.org/10.1016/j.apcatb.2003.11.010.
[5] M. Muruganandham, N. Shobana, M. Swaminathan, Optimization of solar photocatalytic degradation conditions of Reactive Yellow 14 azo dye in

aqueous TiO_2, J. Mol. Catal. A Chem. 246 (1–2) (2006) 154–161, doi:http://dx.doi.org/10.1016/j.molcata.2005.09.052.
[6] M.H. Habibi, A. Hassanzadeh, S. Mahdavi, Photocatalytic degradation of Solophenyl Red 3 BL in an aqueous suspension of titanium dioxide, J. Photochem. Photobiol. A Chem. 172 (1) (2005) 89–96, doi:http://dx.doi.org/10.1016/j.jphotochem.2004.11.009.
[7] C.H. Wu, Photocatalytic degradation and COD removal for indigo carmine dye using aqueous suspension of zinc oxide, Chemosphere 57 (7) (2004) 601–608, doi:http://dx.doi.org/10.1016/j.chemosphere.2004.07.008. 15488922.
[8] M.M. Mohamed, W.A. Bayoumy, M. Khairy, M.A. Mousa, Structural features and photocatalytic behavior of titania and titania supported vanadia synthesized by poly-ol functionalized materials, Micropor. Mesopor. Mater. 109 (1–3) (2008) 445–457, doi:http://dx.doi.org/10.1016/j.micromeso.2007.05.055.
[9] W.D. Wang, P. Serp, P. Kalck, J.L. Faria, Visible light photodegradation of phenol on MWNT–TiO_2 composite catalysts prepared by a modified sol–gel method, J. Mol. Catal. A Chem. 235 (1–2) (2005) 194–199, doi:http://dx.doi.org/10.1016/j.molcata.2005.02.027.
[10] W.C. Oh, A.R. Jung, W.W. Ko, Preparation of fullerene/TiO_2 composite and its photocatalytic effect, J. Ind. Eng. Chem. 13 (2007) 1208–1214.
[11] W.C. Oh, M.L. Chen, Synthesis and characterization of CNT/TiO_2 composites thermally derived from MWCNT and titanium *n*-butoxide, Bull. Korean Chem. Soc. 29 (2008) 159–164.
[12] W.D. Wang, P. Serp, P. Kalck, J.L. Faria, Visible light photodegradation of phenol on MWCNT/TiO2 prepared by a modified sol-gel method, Appl. Catal. B Environ. 56 (4) (2005) 305–312, doi:http://dx.doi.org/10.1016/j.apcatb.2004.09.018.
[13] W.C. Oh, A.R. Jung, W.B. Ko, Characterization and relative photonic efficiencies of a new composite photocatalyst designed for organic dye decomposition and bactericidal activity, Mater. Sci. Eng. C 29 (2008) 1338–1347.
[14] P.C. Ma, B.Z. Tang, J.K. Kim, Effect of CNT decoration with silver nanoparticles on electrical conductivity of CNT–polymer composites, Carbon 46 (11) (2008) 1497–1505, doi:http://dx.doi.org/10.1016/j.carbon.2008.06.048.
[15] V. Georgakilas, D. Gournis, V. Tzitzios, L. Pasquato, D.M. Guldi, M. Prato, Decorating carbon nanotubes with metal or semiconductor nanoparticles, J. Mater. Chem. 17 (26) (2007) 2679–2694, doi:http://dx.doi.org/10.1039/b700857k.
[16] Y.J. An, W.S. Chung, J. Chang, H.C. Lee, Y.R. Cho, Effect of nano-silver particles in bonding material on field emission properties for carbon nanotube cathodes, Mater. Lett. 62 (27) (2008) 4277–4279, doi:http://dx.doi.org/10.1016/j.matlet.2008.06.058.
[17] M.M. Mohamed, M.S. Al-Sharif, Visible light assisted reduction of 4-nitrophenol to 4-aminophenol on Ag/TiO_2 photocatalysts synthesized by hybrid templates, Appl. Catal. B Environ. 142–143 (2013) 432–441.
[18] M.M. Mohamed, K.S. Khairou, Preparation and characterization of nano-silver/mesoporous titania photocatalysts for herbicide degradation, Microporous Mesoporous. Mater. 142 (1) (2011) 130–138, doi:http://dx.doi.org/10.1016/j.micromeso.2010.11.026.
[19] S. Zaki, M.F. El Kady, D. Abd-El-haleem, *Bacillus mojavensis* strain 32A, the use of bioflocculant and bioflocculant-producing *Bacillus mojavensis* strain 32A to synthesize silver nanoparticles *Bacillus mojavensis* strain 32A, the use of bioflocculant and bioflocculant-producing *Bacillus mojavensis* strain 32A to synthesize silver nanoparticles, Mater. Res. Bull. 46 (10) (2011) 1571–1576, doi:http://dx.doi.org/10.1016/j.materresbull.2011.06.025.
[20] I. Sondi, B. Salopek-Sondi, Silver nanoparticles as antimicrobial agent: a case study on *E. coli* as a model for Gram-negative bacteria, J. Colloid Interface Sci. 275 (1) (2004) 177–182, doi:http://dx.doi.org/10.1016/j.jcis.2004.02.012. 15158396.
[21] M.A. Ansari, H.M. Khan, A.A. Khan, M.K. Ahmad, A.A. Mahdi, R. Pal, S.S. Cameotra, Interaction of silver nanoparticles with *E. coli* and their cell envelope biomolecules, J. Basic Microbiol. 54 (9) (2014) 905–915, doi:http://dx.doi.org/10.1002/jobm.201300457. 24026946.
[22] A. Nanda, M. Saravanan, Antimicrobial activity of silver nanoparticles synthesized from novel *Streptomyces* species, Nanomedicine 5 (4) (2009) 369–480.
[23] T.N. Kim, Q.L. Feng, J.O. Kim, J. Wu, H. Wang, G.C. Chen, F.Z. Cui, Antimicrobial effects of metal ions (Ag^+, Cu^{2+}, Zn^{2+}) in hydroxyapatite, J. Mater. Sci. Mater. Med. 9 (3) (1998) 129–134, doi:http://dx.doi.org/10.1023/A:1008811501734. 15348901.
[24] M. Bellantone, H.D. Williams, L.L. Hench, Antimicrobial agents and chemotherapy, Antimicrob. Agents Chemother. 16 (6) (2002) 1940–1945. 12019112.
[25] S.Y. Kwak, S.H. Kim, S.S. Kim, Hybrid organic/inorganic reverse osmosis (RO) membrane for bactericidal anti-fouling. 1. Preparation and characterization of TiO_2 nanoparticle self-assembled aromatic polyamide thin-film-composite (TFC) membrane, Environ. Sci. Technol. 35 (11) (2001) 2388–2394, doi:http://dx.doi.org/10.1021/es0017099. 11414050.
[26] M. Yoshinari, Y. Oda, T. Kato, K. Okuda, Influence of surface modifications to titanium on antibacterial activity in vitro, Biomaterials 22 (14) (2001) 2043–2048, doi:http://dx.doi.org/10.1016/S0142-9612(00)00392-6. 11426884.
[27] M.A. Fox, M.T. Duby, Evaluation of antibacterial effect on *Escherichia coli* PTCC 1395 of TiO_2 nanoparticles synthesized via sol–gel method, Chem. Rev. 93 (1) (1993) 341–357, doi:http://dx.doi.org/10.1021/cr00017a016.
[28] K. Sunada, T. Watanabe, K. Hashimoto, Bactericidal activity of copper-deposited TiO_2 thin film under weak UV light illumination, Environ. Sci. Technol. 37 (20) (2003) 4785–4789, doi:http://dx.doi.org/10.1021/es034106g. 14594392.
[29] P.C. Maness, S. Smolinski, D.M. Blake, Z. Huang, E.J. Wolfrum, W.A. Jacoby, The photocatalytic removal of bacterial pollutants from drinking water, Appl. Environ. Microbiol. 65 (9) (1999) 4094–4098. 10473421.
[30] A. Henglein, Physicochemical properties of small metal particles in solution: "microelectrode" reactions, chemisorption, composite metal particles, and the atom-to-metal transition, J. Phys. Chem. 97 (21) (1993) 5457–5471, doi:http://dx.doi.org/10.1021/j100123a004.
[31] A.P. Alivisatos, Perspectives on the physical chemistry of semiconductor nanocrystals, J. Phys. Chem. 100 (31) (1996) 13226–13239, doi:http://dx.doi.org/10.1021/jp9535506.
[32] G. Fu, P.S. Vary, C.T. Lin, Anatase TiO_2 nanocomposites for antimicrobial coatings, J. Phys. Chem. B 109 (18) (2005) 8889–8898, doi:http://dx.doi.org/10.1021/jp0502196. 16852057.
[33] S.-Y. Wang, S.-Y. Wu, G. Thottappilly, R.D. Locy, N.K. Singh, Different mechanisms of resistance to Bacillus, J. Biosci. Bioeng. 92 (1) (2001) 59–66, doi:http://dx.doi.org/10.1016/S1389-1723(01)80200-0.
[34] J.G.K. Williams, A.R. Kubelik, K.J. Livak, J.A. Rafalski, S.V. Tingey, DNA polymorphisms amplified by arbitrary primers are useful as genetic markers, Nucleic Acids Res. 18 (22) (1990) 6531–6535, doi:http://dx.doi.org/10.1093/nar/18.22.6531. 1979162.
[35] J.G.K. Williams, M.K. Hanafey, J.A. Rafalski, S.V. Tingey, Genetic analysis using random amplified polymorphic DNA markers, Methods Enzymol. 218 (1993) 704–740. 8510556.
[36] M.M. Mohamed, M.S. Al-Sharif, One pot synthesis of silver nanoparticles supported on TiO2 using hybrid polymers as template and its efficient catalysis for the reduction of 4-nitrophenol, Mater. Chem. Phys. 136 (2–3) (2012) 528–537, doi:http://dx.doi.org/10.1016/j.matchemphys.2012.07.021.
[38] G.A. Tompsett, G.A. Bowmaker, R.P. Cooney, J.B. Metson, K.A. Rodgers, J.M. Seakins, Raman study of nanosized titania prepared by sol–gel route, J. Raman Spectrosc. 26 (1) (1995) 57–62, doi:http://dx.doi.org/10.1002/jrs.1250260110.
[39] K.-H. Choi, N. Duraisamy, N.M. Muhammad, I. Kim, H. Choi, J. Jo, Structural and optical properties of electrohydrodynamically atomized TiO_2 nanostructured thin films, Appl. Phys. A 107 (3) (2012) 715–722, doi:http://dx.doi.org/10.1007/s00339-012-6782-0.
[40] N.I. Kovtyukhova, T.E. Mallouk, L. Pan, E.C. Dickey, Individual single walled nanotubes and hydrogels made by oxidative exfoliation of carbon nanotube ropes, J. Am. Chem. Soc. 125 (32) (2003) 9761–9769, doi:http://dx.doi.org/10.1021/ja0344516. 12904042.
[41] N.B. Colthup, L.H. Daly, S.E. Wiberley, Raman Spectroscopy, Academic Press, New York, 1964239–245.
[42] M.G. Gong, X.L. Xu, Z. Yang, Y. Liu, H. Lü, L. Lü, A reticulate superhydrophobic self-assembly structure prepared by ZnO_2 nanowires, Nanotechnology 20 (16) (2009) 165602, doi:http://dx.doi.org/10.1088/0957-4484/20/16/165602. 19420572.
[43] J. Liqiang, S. Xiaojun, X. Baifu, W. Baiqi, C. Weimin, F. Honggang, The preparation and characterization of La doped TiO_2 nanoparticles and their photocatalytic activity, J. Solid State Chem. 177 (10) (2004) 3375–3382, doi:http://dx.doi.org/10.1016/j.jssc.2004.05.064.
[44] Y. Wang, X. Song, S. Shao, H. Zhong, F. Lin, An efficient, soluble, and recyclable multiwalled carbon nanotubes-supported TEMPO for oxidation of alcohols, RSC Adv. 2 (20) (2012) 7693–7698, doi:http://dx.doi.org/10.1039/c2ra21206d.
[45] M.M. Ibrahim, S.A. Ahmed, K.S. Khairou, M.M. Mokhtar, Carbon nanotube/titanium nanotube composites loaded platinum nanoparticles as high performance photocatalysts, Appl. Catal. A 475 (2014) 90–97, doi:http://dx.doi.org/10.1016/j.apcata.2014.01.030.
[46] J. Sun, M. Iwasa, L. Gao, Q.H. Zhang, Single-walled carbon nanotubes coated with titania nanoparticles, Carbon 42 (4) (2004) 895–899, doi:http://dx.doi.org/10.1016/j.carbon.2004.01.074.
[47] P. Wilhelm, D. Stephan, Photodegradation of rhodamine B in aqueous solution via SiO2@TiO2 nano-spheres, J. Photochem. Photobiol. A Chem. 185 (1) (2007) 19–25, doi:http://dx.doi.org/10.1016/j.jphotochem.2006.05.003.
[48] S. Niakan, M. Niakan, S. Hesaraki, M.R. Nejadmoghaddam, M. Moradi, M. Hanafiabdar, Comparison of the antibacterial effects of nanosilver with 18 antibiotics on multidrug resistance clinical isolates of *Acinetobacter baumannii*, Microbiology 6 (5) (2013) e8341–ee8346, doi:http://dx.doi.org/10.5812/jjm.8341.
[49] S.J. Kazmi, M.A. Shehzad, S. Mehmood, A.M.Y. Naeem, A.S. Bhatti, Effect of varied Ag nanoparticles functionalized CNTs on its anti-bacterial activity against E. coli, Sens. Actuators A 216 (2014) 287–294.
[50] A. Amany, S. El-Rab, F. Gad, Effect of reducing and protecting agents on size of silver nanoparticles and their anti-bacterial activity, Der Pharma Chem. 4 (2012) 53–65.
[51] Q.L. Feng, J. Wu, G.Q. Chen, F.Z. Cui, T.M. Kim, G.O. Kim, A mechanistic study of the antibacterial effect of silver ions on *E. coli* and *Staphylococcus aureus*, J. Biomed. Mater Res. 52 (4) (2000) 662–668, doi:http://dx.doi.org/10.1002/1097-4636(20001215)52:4<662::AID-JBM10>3.0.CO;2-3.
[52] S.K. Gogoi, P. Gopinath, A.P. Paul, A. Ramesh, S.S. Ghosh, A. Chattopadhyay, Green fluorescent protein-expressing *E. coli* as a model system for investigating the antimicrobial activities of silver nanoparticles, Langmuir 22 (22) (2006) 9322–9328, doi:http://dx.doi.org/10.1021/la060661v. 17042548.
[53] M.D. Giulio, S.D. Bartolomeo, E.D. Campli, S. Sancilio, E. Marsich, A. Travan, A. Cataldi, L. Cellini, The effect of a silver nanoparticle polysaccharide system on streptococcal and saliva-derived biofilms, Int. J. Mol. Sci. 14 (7) (2013) 13615–13625, doi:http://dx.doi.org/10.3390/ijms140713615. 23812080.